ACS Partner Journal
PRECISION CHEMISTRY

Dual Free Radical Synergism for Enhancing Proton Conductivity in Photochromism iHOFs

Cheng Liu, Xu-Yong Chen,* Xiao-Jie Cao, Wenmin Zhang, and Li-Hui Cao*

Cite This: *Precis. Chem.* 2025, 3, 221−230

Read Online

ACCESS | Metrics & More | Article Recommendations | Supporting Information

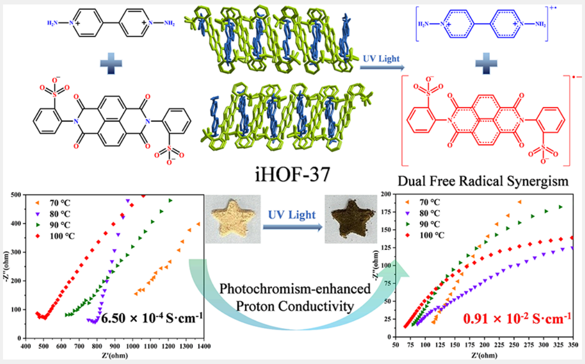

ABSTRACT: Stimuli-responsive smart materials, as an emerging material, can fulfill reversible transformation of chemical/physical properties under external stimuli such as mechanical stress, light, and electricity, which has the highlights of rapid response, designable structure, and function. Two ionic hydrogen-bonded organic frameworks (**iHOFs 36−37**) were synthesized by self-assembly of bis(benzene-*o*/*p*-sulfonic acid)-naphthalenediimide (*o*/*p*-H_2BSNDI) and two basic ligands. The naphthalenediimide (NDI) was introduced into the material to equip **iHOFs 36−37** with radical-driven photochromic behavior. The proton conductivity of **iHOF-37** demonstrated a maximum of 6.50×10^{-4} S·cm^{-1} at 98% RH and 100 °C, and it increased to 9.10×10^{-3} S·cm^{-1} due to dual free radical synergism following UV irradiation (NDI and viologen), which represents a significant 14-fold enhancement. Furthermore, the incorporation of **iHOF-37** into the chitosan (CS) matrix forms photochromic composite membranes. The proton conductivity of the **5%-iHOF-37/CS** composite membrane reached up to 5.70×10^{-2} S·cm^{-1} at 98% RH and 90 °C, and reached 8.08×10^{-2} S·cm^{-1} after UV irradiation. This work reveals the dual radicals generated by NDI and viologen derivatives, whose synergistic action plays a significant role in enhancing the proton conductivity in iHOFs and composite membranes, rendering the rational design of stimuli-responsive smart materials feasible.

KEYWORDS: *ionic HOFs, naphthalenediimine, viologen, photochromism, proton conductivity, crystalline smart material*

■ INTRODUCTION

Crystalline smart materials (CSMs),[1] as a new generation of stimulus-responsive smart materials, have excellent advantages over traditional amorphous materials, such as fast response, designable structure and function, and structure-performance relationships that can be understood at the molecular level through structure.[2−6] It has played an important role in sensors,[7−9] adsorption and separation,[10] chromism,[11−13] smart grids and fuel cells.[14−16] Crystalline porous materials (CPMs) can be characterized and computed by various characterization and calculation methods such as in situ spectroscopy and single-crystal X-ray diffraction/powder X-ray diffraction (SCXRD/PXRD) to determine their exact structures, at the molecular level, to help us understand the mechanisms and structure−property relationships. Current research has focused on metal−organic frameworks (MOFs),[17−20] covalent organic frameworks (COFs)[21−25] and hydrogen-bonded organic frameworks (HOFs),[26−31] whose properties benefit from designable/ordered structure, rich and diverse physicochemical properties, customizable functionalities and tunable pore environments, providing smart materials with new opportunities and a very comprehensive platform.

HOFs are crystalline framework materials formed from organic ligands by intermolecular hydrogen bonding.[32] Their weaker intermolecular hydrogen bonding interactions do make HOFs more responsive when subjected to external stimuli, and well-designed stimulus-responsive HOFs can be responsive to physical/chemical stimuli and exhibit reversible changes in structure, color, luminescence properties and conductivity.[33] However, the weak hydrogen bonding force of it compared to MOFs and COFs leads to insufficient stability, so the stability of it is improved by different strategies: such as $\pi-\pi$ stacking, interpenetration, charge-assisted H-bonds and chemical cross-linking.[34−36] Among them, charge-assisted H-bonds are the more widely used way to improve stability, in which two different organic ligands can give HOFs more properties. HOFs not only possess many advantageous properties of MOFs and COFs, but also have their own unique properties, such as solution processability, and recyclability, which are interesting properties that make HOFs a highly competitive platform for research and applications.[37−40]

Received: December 24, 2024
Revised: February 7, 2025
Accepted: February 11, 2025
Published: February 20, 2025

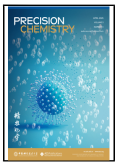

https://doi.org/10.1021/prechem.4c00102

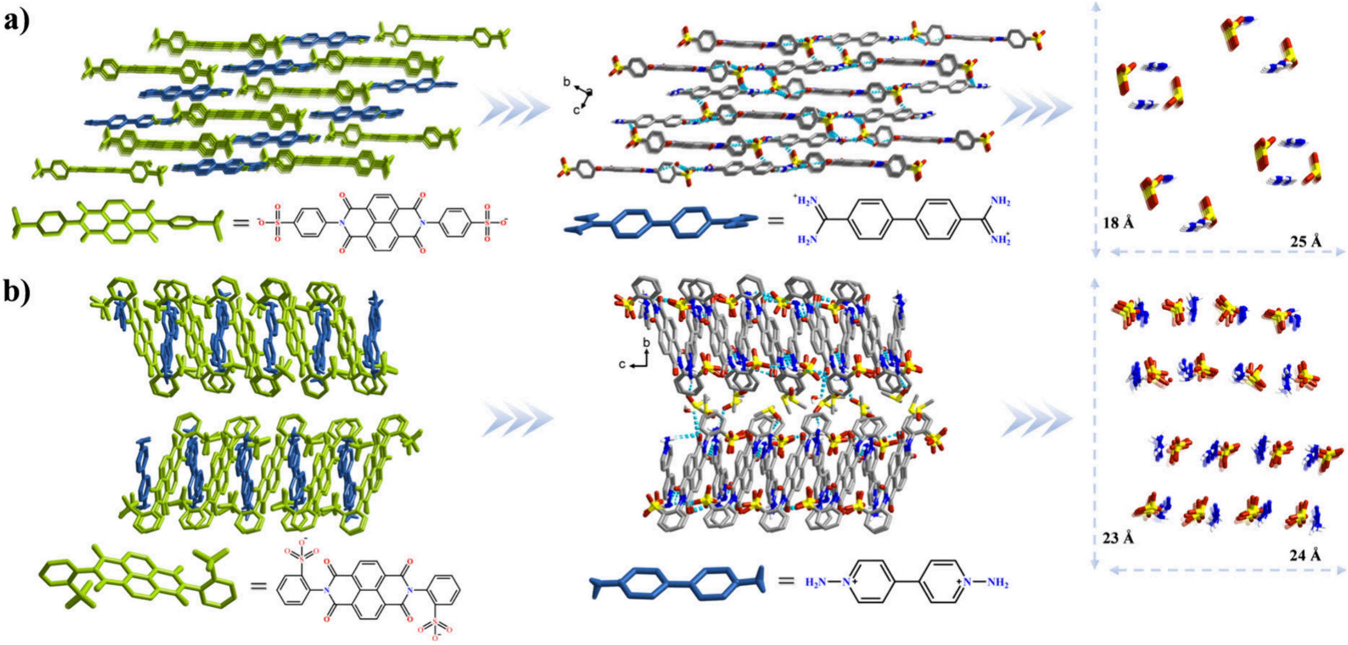

Figure 1. From left to right: schematic diagram, supramolecular structure and number of proton carrier anchors of (a) **iHOF-36**, and (b) **iHOF-37**. Color codes: C, gray; N, blue; H, white; O, red; S, yellow. Some hydrogen atoms, solvent molecules, and ligand molecules have been omitted for clarity.

Increasing the quantity of proton carriers and bringing in a higher number of acidic functional groups,[41,42] such as carboxylic acids,[43,44] sulfonic acids,[45,46] or phosphoric acids, is an effective way to increase proton conductivity. The presence of acidic functional groups not only increases the proton transport sites of the material, but also enriches the hydrogen bonding network of the structure.[47−49] Introducing stimuli-responsive groups into HOFs to change the microenvironment of the structure when stimulated by external conditions, thereby increasing the proton conductivity of the material, is also an effective strategy. Photoinduced Electron-Transfer (PIET)[50] involves the introduction of light-responsive groups into the material's structural framework, thereby facilitating the expeditious delivery of the material's light signal to specific locations, resulting in the acquisition of photochromic and light-modulated plasmonic conductivity properties.

Herein, we synthesized two ionic HOFs (**iHOFs 36−37**) by self-assembly of bis(benzene-*o*/*p*-sulfonic acid)-naphthalenediimide (*o*/*p*-H_2BSNDI) and two types of basic ligands. The NDI[51] was introduced into the material framework to endow **iHOFs 36−37** with radical-driven photochromic behaviors, unlike **iHOF-36**, one of the components in **iHOF-37** was a viologen derivative, which allows it to generate dual radicals upon light irradiation. The photogenerated radical-induced proton conductivity of **iHOF-36** was enhanced by 2.2−3.6 times at 85% RH and 60−100 °C. The proton conductivity of **iHOF-37** peaked 6.50×10^{-4} S·cm^{-1} at 98% RH and 100 °C, and it rose to 9.10×10^{-3} S·cm^{-1} due to dual free radical synergism after UV irradiation, which was representing a significant 14-fold enhancement. Additionally, **iHOF-37** was incorporated into a chitosan (CS) matrix and formed photochromic composite membranes. The proton conductivity of **5%-iHOF-37/CS** composite membrane reached up to 5.70×10^{-2} S·cm^{-1} at 98% RH and 90 °C, and reached 8.08×10^{-2} S·cm^{-1} after UV irradiation. This study reveals the significant role of the synergistic effect of dual free radicals generated by NDI and viologen derivatives in enhancing the proton conductivity in iHOFs and composite membranes.

RESULTS AND DISCUSSION

Crystal Structure Descriptions

iHOFs 36−37 were synthesized by self-assembly of bis(benzene-*o*/*p*-sulfonic acid)-naphthalenediimide (*o*/*p*-H_2BSNDI) by reaction with 1,1′-diamino-4,4′-bipyridine diiodide (DBpy·2I) and [1,1′-biphenyl]-4,4′-bis(carboximidamide) dihydrochloride (BPAM·2HCl), respectively.

iHOF-36 has been analyzed by SCXRD to reveal that the structural formula is $[H_2(BPAM)]$ (*p*-BSNDI)·($5H_2O$), belonging to the triclinic crystal system with the space group *P*-1. The asymmetric unit contains one *p*-BSNDI^{2-} anion, one in situ protonated $[H_2(BPAM)]^{2+}$ cation, and five free water molecules (Figure S1). We observe that these units assemble into a three-dimensional supramolecular network structure through hydrogen bonding interactions, as shown in Figure 1a. Viewed from the *a*-axis, the *p*-BSNDI^{2-} anions and $[H_2(BPAM)]^{2+}$ cations are alternately arranged in each layer, forming organic ligand chains. The chains in the first and second layers are interconnected through hydrogen bonds formed by sulfonic acid groups, amidine groups, water molecules, and the O atoms on the two NDI core carbonyl groups, resulting in two types of hydrogen-bonded rings, designated as ① and ② (Figure S2). In structures ① and ②, the sulfonic acid groups, carbonyl groups, and O atoms of H_2O on *p*-BSNDI^{2-} are interconnected with the H atoms on H_2O and $[H_2(BPAM)]^{2+}$ through hydrogen bonding, forming distinct one-dimensional hydrogen-bonded tubular structures (Figure S3).

iHOF-37 has been analyzed by SCXRD to reveal that the structural formula is (DBpy) (*o*-BSNDI)·(DMSO)·(H_2O), belonging to the monoclinic crystal system with the space

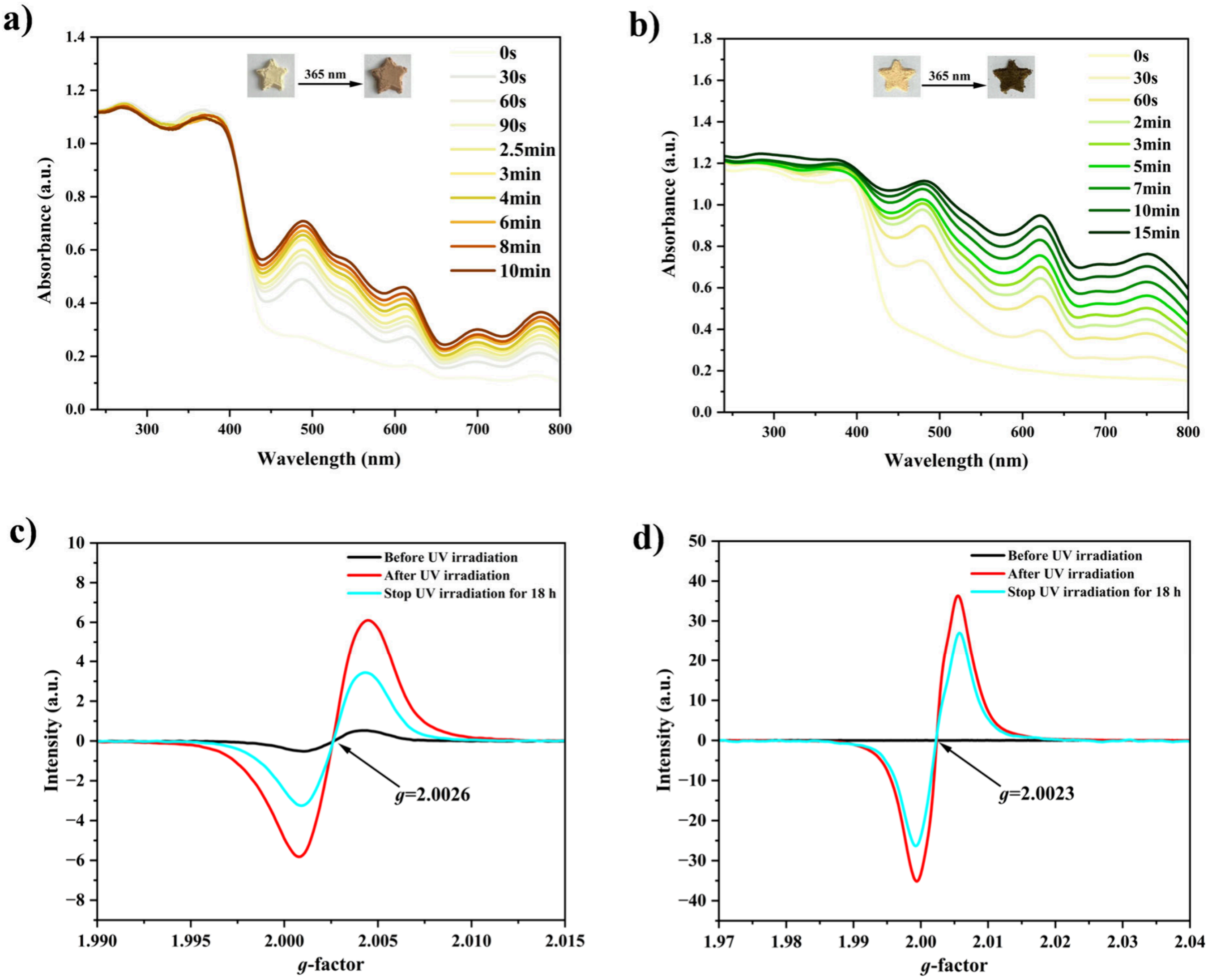

Figure 2. UV−vis spectrum of the crystalline powder discoloration process of (a) **iHOF-36** and (b) **iHOF-37**. Inset: corresponding color changes before and after irradiation. EPR spectra of (c) **iHOF-36** and (d) **iHOF-37** before and after 365 nm UV irradiation and after 18 h of irradiation.

group $P2_1/c$. As shown in Figure S5, the asymmetric unit consists of six *o*-BSNDI^{2-} ions, six DBpy^{2+} ions, two guest water molecules, and seven DMSO molecules. As shown in Figures 1b and S4, viewed from the *a*-axis, the *o*-BSNDI^{2-} anions and DBpy^{2+} cations are alternately arranged in each layer, forming organic ligand molecular chains. In each chain, the sulfonic acid groups, carbonyl groups, and solvent molecules (H_2O and DMSO) on *o*-BSNDI^{2-} are interconnected with the H atoms of DBpy^{2+} and H_2O through hydrogen bonds. Additionally, the solvent molecules of DMSO and water interspersed in the voids are connected to the adjacent chains above and below through hydrogen bonds, extending infinitely to form a three-dimensional supramolecular network structure.

Through the analysis in Figure 1b, we found that there are multiple highly ordered hydrogen bonding interactions in **iHOF-37**, which positively contribute to the stability of the crystal structure. When the crystal phase is viewed along the crystallographic *a*-axis, the staggered arrangement of NDI and amine molecules leads to a densely packed crystalline phase and an intensive hydrogen bonding network, exhibiting a high density of hydrogen bonds. Correlating the hydrogen bonds with the number of proton carriers, namely amine and sulfonic acid groups, there are numerous proton donors and acceptors within an area of 24 Å in length and 23 Å in width, which facilitates proton binding and transport. In contrast, as seen from Figure 1a, the structure of **iHOF-36** has a lower density of hydrogen bonds. Moreover, the number of proton carriers within an area of 25 Å in length and 18 Å in width is significantly less than that in **iHOF-37**. Therefore, we infer that **iHOF-37** is more favorable for proton transport. Detailed crystallographic data for **iHOFs 36−37** are provided in Table S1, and hydrogen bonds data are listed in Tables S2−S3. ^{1}H NMR and FTIR spectrum of **iHOFs 36−37** are shown in Figures S6−S9.

Photochromic Study

The freshly prepared crystals are continuously exposed to a UV light source; the color of **iHOF-36** changes from its initial beige to orange-red (Figure S17a), while **iHOF-37** changes from yellow to dark green (Figure S17b). Upon heating these color-changed powders to 120 °C and maintaining this temperature for approximately 6 h, we observed that the colors largely revert to their original states (Figure S18). To

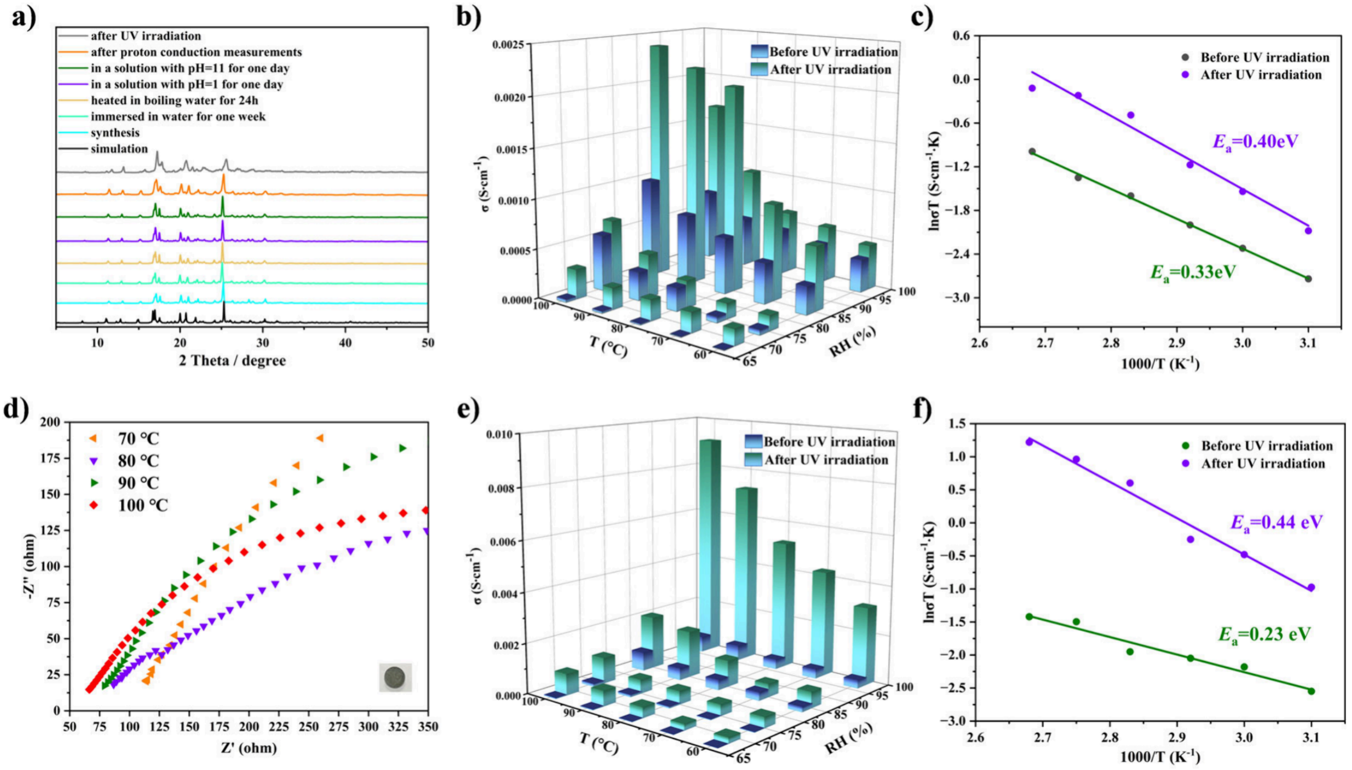

Figure 3. (a) PXRD of **iHOF-36**. Proton conductivity (S·cm^{-1}) of (b) **iHOF-36**, and (e) **iHOF-37** before and after discoloration at 60−100 °C and different RH. (c) Arrhenius plots of **iHOF-36** before and after discoloration at 85% RH and 50−100 °C. (d) Nyquist plot of **iHOF-37** at 98% RH. (f) Arrhenius plots of **iHOF-37** before and after discoloration at 98% RH and at 50−100 °C.

assess the structural stability of the crystals during the photochromic process, we conducted PXRD and Fourier transform infrared (FTIR) spectrum analyses before and after the color change (Figures S10−S13). Since there is no change in the crystal morphology, it indicates that the structure remains stable.

The UV−vis absorption spectrum further confirmed the photochromism of **iHOFs 36−37**. Prior to UV irradiation, the **iHOF-36** sample exhibited significant absorption in the UV region, and four new broad absorption peaks appeared at 488, 612, 699, and 780 nm in the visible region after UV irradiation. As the irradiation time increases, the intensity of the absorption bands in the ultraviolet region and at these wavelengths continues to increase, and these peaks may be characteristic of the photogenerated radicals. When the UV light source was removed, the absorption bands gradually weakened (Figure 2a). **iHOF-37** exhibits a similar behavior, with the difference being that after UV irradiation, three new broad absorption peaks appear at 480, 624, and 756 nm in the visible light region, accompanied by a change in appearance to a deep green color (Figure 2b), and saturation was reached after 15 min.

Analysis of the crystals by an electron paramagnetic resonance (EPR) spectrum revealed that no free radical signals were detected in either crystal before UV irradiation. However, **iHOFs 36−37** exhibited significant radical signals with g-factors of 2.0026 and 2.0023 after UV irradiation, respectively (Figure 2c,d). These results indicate that the color change is caused by electron transfer following UV irradiation, resulting in the formation of NDI-centered radical anions. As observed in the EPR spectrum, the intensity of the radical signals in the crystals significantly increases after UV irradiation.

Stability Studies of Crystals

Prior to exploring the proton conductivity of these crystals, we conducted a comprehensive stability study. Freshly prepared 15 mg samples of **iHOFs 36−37** were soaked in water for 24 h or a week, in boiling water, and in aqueous solutions with pH values of 1 and 11 for 24 h, respectively, followed by drying. PXRD analysis revealed that the experimental PXRD patterns were highly correlated with the simulated patterns (Figures 3a and S13), indicating that both samples exhibited good stability in water, acidic, and alkaline environments.

Furthermore, we employed thermogravimetric analysis (TGA) to monitor the stability of the crystals in an air atmosphere within the temperature range 25−800 °C. As illustrated in Figures S14−S15, the analysis indicated that the thermal decomposition temperatures of these samples were very close, demonstrating that the crystals exhibited excellent thermal stability. From the TGA curves, it is evident that **iHOF-36** began to lose weight at 35 °C, which suggests that the hydrogen bonds within the crystal are relatively strong. The mass decrease within the range of 35 to 170 °C was due to the evaporation of crystalline water molecules. For **iHOF-37**, the mass decrease trend within the range of 35 to 200 °C was due to the combined loss of H_2O and DMSO.

Proton Conductivity Properties

The unique structural features and photochromic behavior exhibited by these iHOFs inspired us to further explore their proton conductivity properties in the solid state.

Taking **iHOFs 36−37** as the objects of study, we pressed the powder of these samples into thin sheets at 5 MPa. Subsequently, we employed electrochemical impedance spectroscopy (EIS) to comprehensively test the proton con-

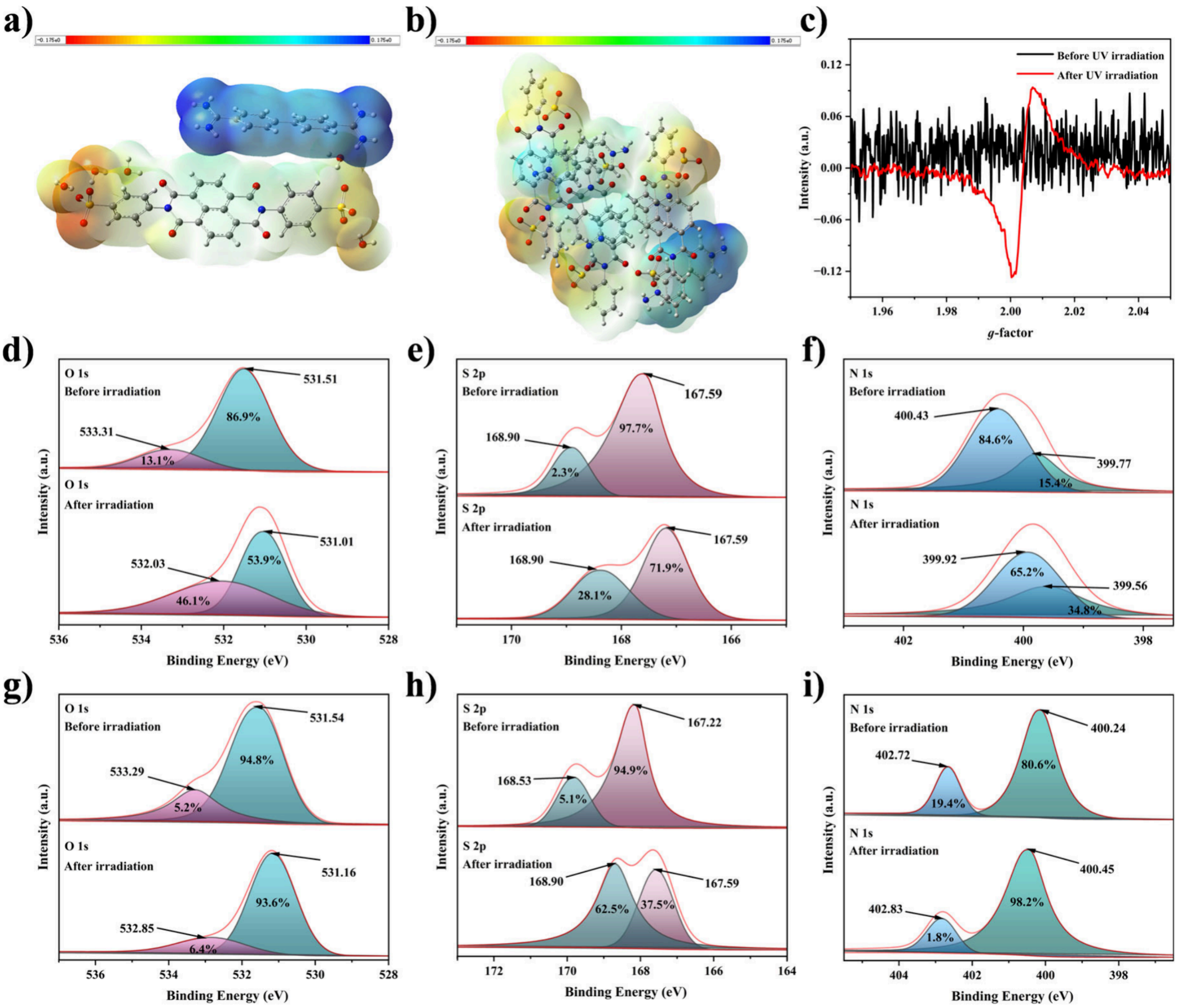

Figure 4. Electrostatic potential (ESP) of (a) **iHOF-36**, and (b) **iHOF-37** crystals between −0.175 eV (red) and 0.175 eV (blue). (c) EPR spectrum of the $[\text{DBpy}]^{+\cdot}$ free radical before and after 365 nm UV irradiation. XPS spectra of **iHOF-36** before and after light exposure for (d) O 1s, (e) S 2p and (f) N 1s. XPS spectra of **iHOF-37** before and after light exposure for (g) O 1s, (h) S 2p and (i) N 1s.

ductivity of these sheets under different relative humidity conditions (68%−98% RH) and temperature ranges (60−100 °C). The proton conductivity of **iHOF-36** was enhanced significantly from 2.86×10^{-4} to 1.00×10^{-3} S·cm^{-1} with increasing temperature at 85% RH, an improvement of about 3.5-fold (Figure S23). Similarly, the proton conductivity of **iHOF-37** was enhanced with increasing temperature from 3.40×10^{-4} to a remarkable 6.50×10^{-4} S·cm^{-1} at 98% RH (Figure S25). We speculate that as the temperature and RH were increased, more water molecules may penetrate into the material, thereby disrupting the proton transport pathways. Therefore, we did not include these data in our statistical analysis. By analyzing the PXRD patterns in Figures 3a and S12−S13, we found that both **iHOFs 36−37** maintained structural stability after exposure to water vapor. The proton conductivity data are detailed in Figure 3b,e and Tables S4−S5. These test results indicate that their proton conductivity is positively correlated with both temperature and RH. The increase in proton conductivity with rising RH may be attributed to an increase in the number of proton transport channels within the sample, leading to a reduction in resistance. These test results indicate that their proton conductivity is positively correlated with temperature and RH. To further investigate the proton conduction mechanism, we recognized that the activation energy (E_a) is crucial for understanding the potential of proton migration. Therefore, we calculated the activation energy based on the Arrhenius equation. The activation energy of **iHOF-36** at 85% RH and 100 °C was 0.33 eV (Figure 3c), and the activation energy of **iHOF-37** at 98% RH and 100 °C was 0.25 eV (Figure 3f). when $E_a < 0.4$ eV, which is consistent with the typical *Grotthuss mechanism*,[52,53] suggesting that the high-density hydrogen bonding network inside the crystal promotes the proton hopping migration, which effectively reduces the potential barriers during proton migration and consequently lowers the E_a.

In an effort to investigate the effect of radicals generated during the light-induced electron transfer process on proton

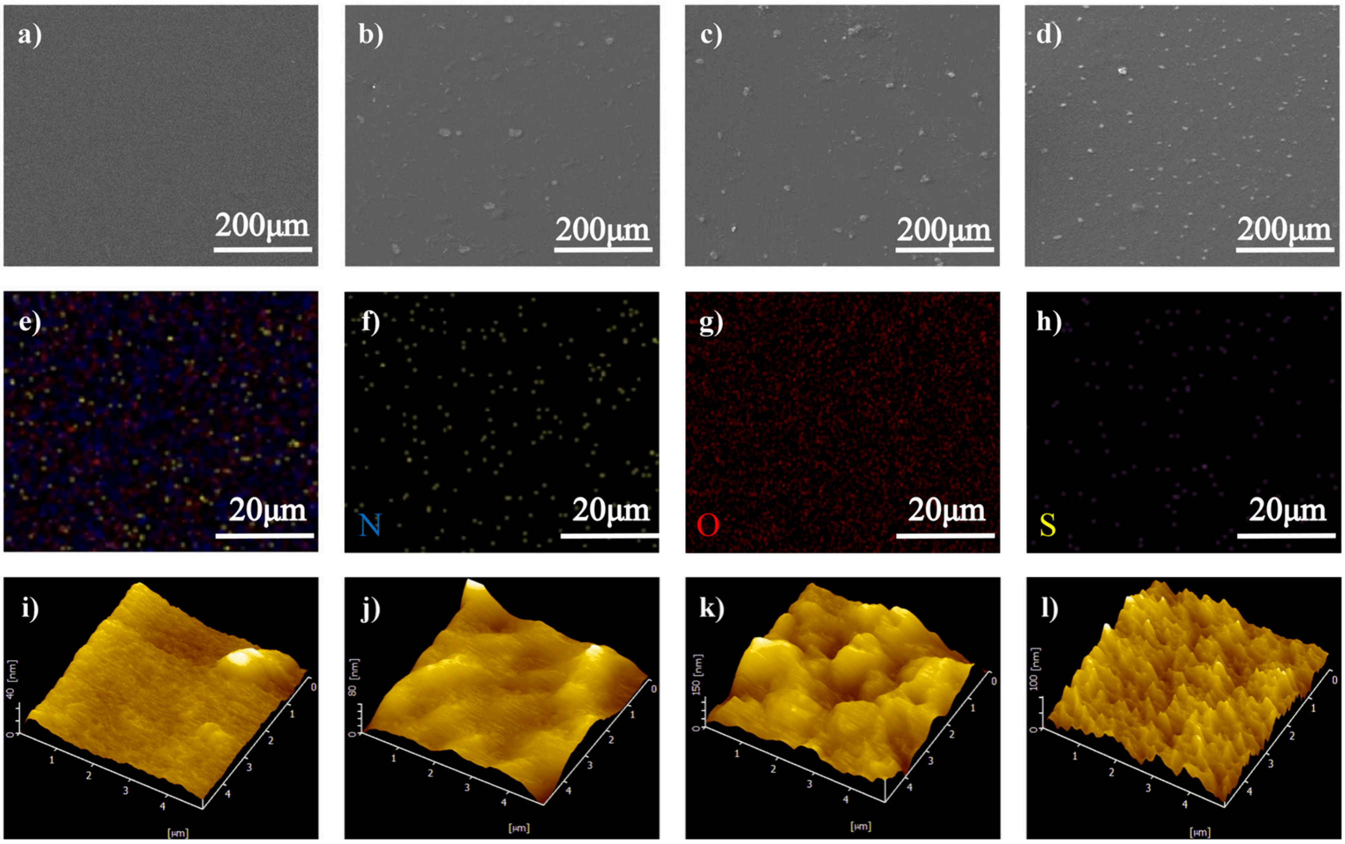

Figure 5. (a-d) SEM images of **X-iHOF-37/CS** (X = 0%, 1%, 3%, 5%) composite membranes. (e-h) Total elemental distribution map of the **5%-iHOF-37/CS** membrane and the image mapping of elements corresponding to N, O and S in the membrane. (i-l) AFM topography images of **X-iHOF-37/CS** (X = 0%, 1%, 3%, 5%) composite membranes.

conduction behavior, we conducted electrochemical impedance measurements on **iHOFs 36−37** samples that had been exposed to UV light following the same procedure as before. The samples before and after light exposure exhibit similar temperature-dependent proton conduction characteristics. As shown in Table S4 and Figure S24, the proton conductivity of **iHOF-36** was enhanced from 6.43×10^{-4} to 2.39×10^{-3} S·cm^{-1} with increasing temperature at 85% RH, an improvement of about 3.7-fold. Comparing the proton conductivity before and after discoloration at 100 °C and 85% RH, we calculated that the proton conductivity on/off ratio was 2.39. It was noteworthy that in the structure of **iHOF-37**, there exist anions centered on NDI and bipyridinium cations, which undergo electron transfer upon light induction to form stable dual free radical. Their synergistic effect plays a crucial role in enhancing the proton conductivity. The proton conductivity of UV-irradiated **iHOF-37** was enhanced with increasing temperature from 3.12×10^{-3} to a remarkable 9.10×10^{-3} S·cm^{-1} at 98% RH (Figure S26). Comparing the proton conductivity before and after discoloration at 100 °C and 98% RH, we obtained that the maximum proton conductivity on/off ratio was 14, and its proton conductivity amplitude can reach 9−12 times at different temperatures (Figure 3b,d,e). As shown in the purple patterns (Figure 3c,f), the E_a of UV-irradiated **iHOFs 36−37** were 0.40 and 0.44 eV, respectively, a result which suggests that the proton conduction in the structure may be a hybrid mechanism of both the *Grotthuss mechanism* and the *Vehicle mechanism* hybrid mechanism. Specifically, at low temperatures and low RH, proton conductance was more inclined to follow the *Grotthuss mechanism*, whereas at low RH and high temperatures or high RH, proton conductance was more likely to favor the Vehicle mechanism due to the high presence of H_3O^+. In summary, the proton conductivity of **iHOFs 36−37** was significantly enhanced, possibly due to the formation of stable radicals after light irradiation. Therefore, we conducted a study of its mechanism.

Mechanistic Studies

The electrostatic potential (ESP) of **iHOFs 36−37** was calculated by the Gaussian 09 program (b3lyp/6-311 + g(d) smd). The analysis of the results in Figure 4a,b indicates that the initial electrons of **iHOFs 36−37** are primarily concentrated around the oxygen atoms of the NDI core's carbonyl and sulfonic acid groups, as well as the sulfur atom of the sulfonic acid group. Notably, **iHOF-37** exhibits a broader electron distribution and higher electron density compared to **iHOF-36**, suggesting that its initial electron density is significantly greater. In the EPR tests, we observed that both sulfonate ligands, *p*-H_2BSNDI and *o*-H_2BSNDI, exhibited distinct radical signals, with the latter showing a higher signal intensity than the former (Figures S19−S20). Given that the DBpy·2I compound is a viologen derivative, during the photoinduced electron transfer process, the DBpy^{2+} cation acquires an electron to form a viologen radical cation (Figure 4c). Combining these results with those from Figure 2c,d, we conclude that **iHOF-36** exhibits single radical characteristics, while **iHOF-37** demonstrates a synergistic effect of double radicals.

During the exposure period, the electron transfer process of **iHOF-36** was analyzed. *p*-H_2BSNDI consists of two π-

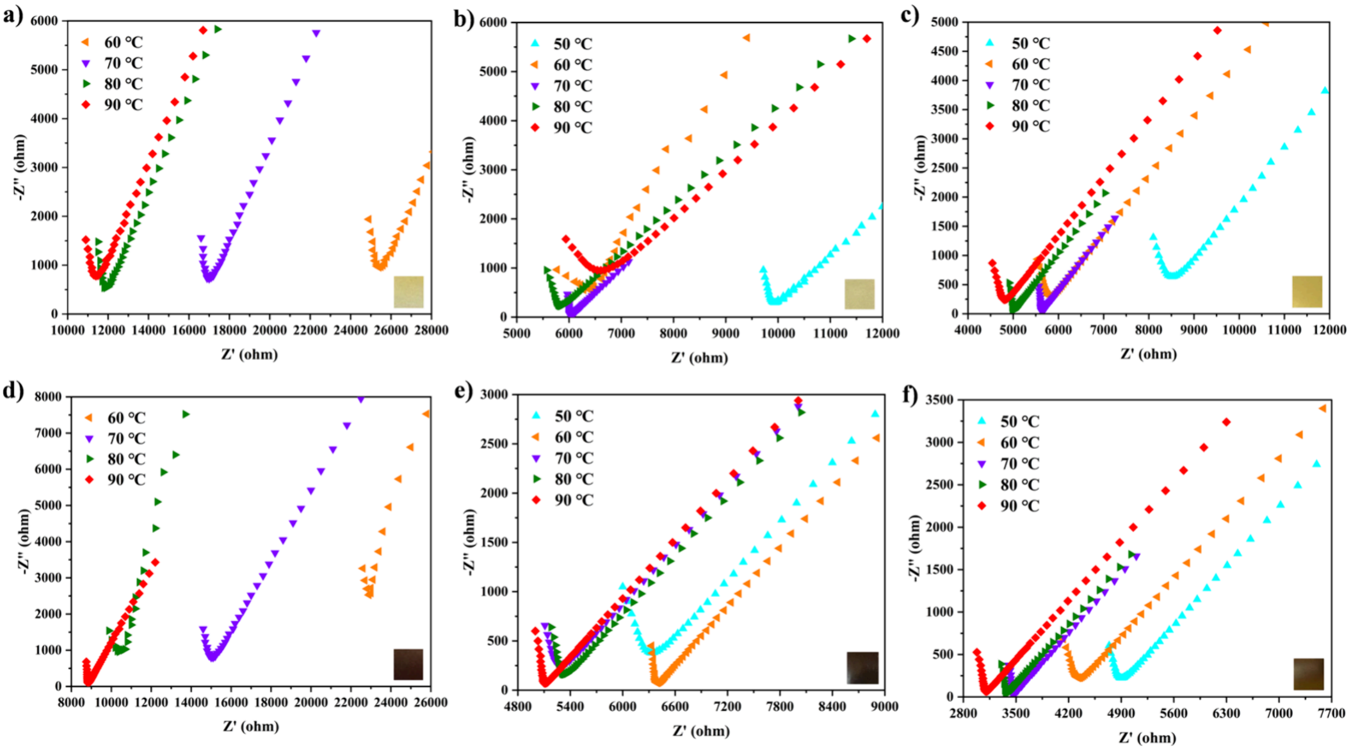

Figure 6. (a-c) Nyquist plot before UV irradiation of **X-iHOF-37/CS** (X = 1%, 3%, 5%) at 98% RH and different temperature. (d-f) Nyquist plot after UV irradiation of **X-iHOF-37/CS** (X = 1%, 3%, 5%) at 98% RH and different temperature.

electron-rich benzenesulfonate centers and one electron-deficient naphthalenediimide center. It is speculated that the sulfonate groups, in conjunction with H_2O, act as electron donors. Upon stimulation with 365 nm UV light, electrons are initially transferred from these donors to the $[H_2(BPAM)]^{2+}$ cation, and subsequently from $[H_2(BPAM)]^{2+}$ to the NDI center, ultimately forming a radical anion centered on NDI. To confirm the electron transfer processes in **iHOFs 36−37**, XPS analysis was conducted. The XPS spectra of the peaks of O 1s, S 2p, and N 1s are shown in Figure 4d-i. After exposure to 365 nm UV light in **iHOF-36**, as seen in Figure 4d-f, an increase in the area of the high binding energy peak near 531.31 eV in the O 1s spectrum was observed. Additionally, an increase in the area of the binding energy peak near 168.90 eV in the S 2p spectrum was noted, indicating electron loss from the O and S atoms. In the N 1s spectrum, a decrease in the area of the high binding energy peak near 400.43 eV suggests that the N atom has gained electrons.

Similarly, the electron transfer process in **iHOF-37** was analyzed. The composition of *o*-H_2BSNDI in **iHOF-37** is similar to that in **iHOF-36**. It is speculated that the sulfonate groups, in conjunction with solvent H_2O/DMSO, act as electron donors, providing electrons to the $DBpy^{2+}$ cation upon stimulation with 365 nm UV light, prompting its conversion to the $[DBpy]^{+\cdot}$ radical cation. Subsequently, electrons are further transferred to the NDI center, forming a radical anion centered on NDI. This process ultimately leads to the formation of a double radical synergistic mechanism. The XPS spectra of **iHOF-37** are shown in Figures 4g-i. An increase in the area of the high binding energy peak near 533.29 eV in the 1s-O spectrum and an increase in the area of the binding energy peak near 168.53 eV in the 2p-S spectrum were observed. Additionally, compared to the O 1s spectrum of **iHOF-36**, the increase in the peak area of the O atom was lower, which we attribute to the formation of the viologen radical cation as the bipyridinium cation gains electrons. These observations indicate electron loss from the O and S atoms. In the N 1s spectrum, a decrease in the area of the high binding energy peak near 402.72 eV suggests that the N atom gained electrons. Based on this comprehensive analysis, we conclude that **iHOF-37** exhibits superior electron transfer capability compared to **iHOF-36**, which is more favorable for proton conduction, enhancing the proton conductivity. These diagrams indicate the distribution of ESP potential values for **iHOFs 36−37** (Figures S21−S22).

Membrane Characterization

Chitosan (CS) possesses excellent film-forming ability and hydrophilicity, so we doped crystals into it to obtain **X-iHOF-37/CS** composite membranes (X = 1%, 3%, 5%). We conducted in-depth research on their morphology, flexibility, water absorption and swelling, proton conductivity, and other properties. We conducted a detailed analysis of the microstructure of the composite membranes using scanning electron microscopy (SEM) and atomic force microscopy (AFM). The SEM images clearly indicate that the crystal particles are evenly distributed within the CS matrix, and as the crystal content increases, the surface roughness of the membrane also increases (Figures 5a-d and S28). Furthermore, an energy dispersive spectroscopy (EDS) analysis was conducted on the **5%-iHOF-37/CS** membrane to investigate the element distribution (Figure 5e-h). It was found that N, O, and S (with S originating from the crystals and N, and O from both the crystals and CS) are uniformly distributed within the CS matrix, forming a dense and homogeneous composite membrane material. The AFM images (Figure 5i-l) indicate that the surface of the pure CS membrane is smoother, and the surface roughness of the membrane increases with the increase in crystal doping concentration.

The thermal stability of the membranes was investigated using TGA. From the data analysis in Figure S16, it is observed that the membranes initially undergo a gradual mass loss between 35 and 180 °C, primarily due to the evaporation of H_2O and DMSO within the membranes. The second stage of mass loss, observed between 180 and 250 and 250−350 °C, is attributed to the thermal decomposition of $-SO_3H$ groups. Compared to the pure CS membrane, the overall thermal stability of the composite membranes gradually increases with the increasing doping ratio of the crystals.

Tensile tests were conducted on the membranes to obtain their stress−strain curves (Figure S27). Compared with the pure CS membrane, the composite membranes containing **iHOF-37** exhibited good mechanical stability at various doping ratios. The water uptake and swelling degree are related to tensile properties. To investigate the impact of crystals on the water retention and dimensional changes of the membranes, water absorption and swelling experiments were conducted (Table S8). The experimental results indicate that the incorporation of crystals has a negative effect on the water absorption and swelling characteristics of the membranes. Compared with the pure CS membrane, as the crystal content increases, both the water absorption and swelling ratios of the membranes decrease. The **5%-iHOF-37/CS** membrane exhibits the lowest water absorption and swelling ratios, with a water absorption ratio of 26.32% and a swelling ratio of 18.65%. Ion exchange capacity (IEC) is a crucial indicator for evaluating the number of exchangeable ions in PEMs, primarily referring to sulfonic acid groups. Generally, the higher the IEC value of PEMs, the better their proton conductivity. We determined the IEC of the membranes using acid−base titration (Table S8) and found that the IEC value of the membranes increased with the increasing crystal content.

Proton Conductive Properties of Membranes

Proton conductivity is one of the fundamental parameters for evaluating the performance of the PEMs. The incorporation of **iHOF-37** into chitosan (CS) matrix forms photochromic composite membranes and EIS tests were conducted.

As shown in Figures 6a-c, S29−S30 and Table S6, the proton conductivity of the pure CS membranes was 1.39×10^{-2} S·cm^{-1} at 98% RH and 90 °C, the proton conductivity was significantly enhanced with the increase of the doping ratio of **iHOF-37**, when doped at 5%, the proton conductivity was enhanced with increasing temperature from 2.85×10^{-2} to a remarkable 5.70×10^{-2} S·cm^{-1}. The color-changed membrane was subjected to EIS testing under 98% RH (Table S6 and Figure 6d-f) the proton conductivity significantly increased from 5.70×10^{-2} to 8.08×10^{-2} S·cm^{-1}. Comparing the proton conductivity of membranes with different doping ratios before and after UV irradiation at 90 °C and 98% RH, we calculated the optical on/off ratios of proton conductivity to be 1.22, 1.12, and 1.42 for doping levels of 1%, 3%, and 5% crystals, respectively. The E_a was 0.19 and 0.11 eV before and after discolouration of **5%-iHOF-37/CS** at 98% RH and 90 °C, respectively (Figure S31), and they were both *Grotthuss mechanisms*. Statistics are available on the relationship between the proton conductivity of membranes with different doping ratios and that of pure CS membranes (Table S7). The proton conductivity of photoconductive materials with photochromic properties reported in the literature was compiled and analyzed (Table S9).

CONCLUSIONS

In summary, by strategic design, we successfully constructed two charge-assisted HOFs named **iHOFs 36−37** based on two types of basic ligands and bis(benzene-*o*/*p*-sulfonic acid)-naphthalenediimide (*o*/*p*-H_2BSNDI). The NDI was introduced into the material to endowed **iHOFs 36−37** with radical-driven photochromic behaviors, and the photochromicity was confirmed by UV−vis, EPR, unlike **iHOF-36**, one of the components in **iHOF-37** was a viologen derivative, which allows it to generate dual free radicals upon light irradiation. The photogenerated radical-induced proton conductivity of **iHOF-36** was enhanced by 2.2−3.6 times at 85% RH and 60−100 °C. The proton conductivity of **iHOF-37** peaked at 6.50×10^{-4} S·cm^{-1} at 98% RH and 100 °C, it rose to 9.10×10^{-3} S·cm^{-1} due to dual free radical synergism after UV irradiation, which was representing a significant 14-fold enhancement. Meanwhile, **iHOF-37** with a highly ordered hydrogen bonding network was doped into the CS matrix to polymerize into a membrane, which effectively improved the comprehensive performance of the composite membrane. The proton conductivity of the **5%-iHOF-37/CS** composite membrane reached 5.70×10^{-2} S·cm^{-1} at 98% RH and 90 °C, and the proton conductivity was enhanced by about 1.42-fold after UV irradiation compared with that to 8.08×10^{-2} S·cm^{-1} before irradiation. As a result, the present work demonstrates compounds with photochromic and photo-induced modulated proton conduction properties, providing ideas and methods for the design and development of multifunctional and smart crystalline materials with diverse photochromic properties, and tunable proton conduction.

ASSOCIATED CONTENT

Supporting Information

The Supporting Information is available free of charge at https://pubs.acs.org/doi/10.1021/prechem.4c00102.

Crystallographic data for **iHOF-36** (CIF)

Crystallographic data for **iHOF-37** (CIF)

Materials, experimental details, crystal data, crystal structures, proton conductivity, ^{1}H NMR, FTIR, PXRD, TGA, EPR (PDF)

AUTHOR INFORMATION

Corresponding Authors

Xu-Yong Chen − *Shaanxi Key Laboratory of Chemical Additives for Industry, College of Chemistry and Chemical Engineering, Shaanxi University of Science and Technology, Xi'an 710021, P. R. China*; Email: chenxuyong@sust.edu.cn

Li-Hui Cao − *Shaanxi Key Laboratory of Chemical Additives for Industry, College of Chemistry and Chemical Engineering, Shaanxi University of Science and Technology, Xi'an 710021, P. R. China*; orcid.org/0000-0002-3676-0242; Email: caolihui@sust.edu.cn

Authors

Cheng Liu − *Shaanxi Key Laboratory of Chemical Additives for Industry, College of Chemistry and Chemical Engineering,* *Shaanxi University of Science and Technology, Xi'an 710021, P. R. China*

Xiao-Jie Cao − *Shaanxi Key Laboratory of Chemical Additives for Industry, College of Chemistry and Chemical Engineering, Shaanxi University of Science and Technology, Xi'an 710021, P. R. China*

Wenmin Zhang − *Department of Chemical Engineering and Food Science, Zhengzhou University of Technology, Zhengzhou 450044 Henan Province, China*

Complete contact information is available at: https://pubs.acs.org/10.1021/prechem.4c00102

Author Contributions

Cheng Liu, data curation, formal analysis, investigation, writing-original draft; synthesis, single crystal testing and ionic conductivity testing were performed by Xu-Yong Chen and Xiao-Jie Cao; Li-Hui Cao, conceptualization, funding acquisition, supervision, review and editing; Wenmin Zhang, funding acquisition and review. All the authors approved the final version of the article.

Notes

The authors declare no competing financial interest.

■ ACKNOWLEDGMENTS

This work was supported by the National Natural Science Foundation of China (22302180 and 22075169), Shaanxi Fundamental Science Research Project for Chemistry and Biology (22JHQ026), and Shaanxi University of Science and Technology.

■ REFERENCES

(1) Yan, D.; Wang, Z.; Zhang, Z. Stimuli-Responsive Crystalline Smart Materials: From Rational Design and Fabrication to Applications. *Acc. Chem. Res.* **2022**, *55*, 1047−1058.

(2) Chen, X.-Y.; Cao, L.-H.; Bai, X.-T.; Cao, X.-J. Charge-Assisted Ionic Hydrogen-Bonded Organic Frameworks: Designable and Stabilized Multifunctional Materials. *Chem.—Eur. J.* **2024**, *30*, No. e202303580.

(3) Li, Y.; Sui, J.; Cui, L.-S.; Jiang, H.-L. Hydrogen Bonding Regulated Flexibility and Disorder in Hydrazone-Linked Covalent Organic Frameworks. *J. Am. Chem. Soc.* **2023**, *145*, 1359−1366.

(4) Lal, G.; Derakhshandeh, M.; Akhtar, F.; Spasyuk, D. M.; Lin, J.-B.; Trifkovic, M.; Shimizu, G. K. H. Mechanical Properties of a Metal−Organic Framework formed by Covalent Cross-Linking of Metal−Organic Polyhedra. *J. Am. Chem. Soc.* **2019**, *141*, 1045−1053.

(5) Chen, X.; Geng, K.; Liu, R.; Tan, K. T.; Gong, Y.; Li, Z.; Tao, S.; Jiang, Q.; Jiang, D. Covalent Organic Frameworks: Chemical Approaches to Designer Structures and Built-In Functions. *Angew. Chem., Int. Ed.* **2020**, *59*, 5050−5091.

(6) Zhang, J.; Han, X.; Wu, X.; Liu, Y.; Cui, Y. Multivariate Chiral Covalent Organic Frameworks with Controlled Crystallinity and Stability for Asymmetric Catalysis. *J. Am. Chem. Soc.* **2017**, *139*, 8277−8285.

(7) Li, S.-L.; Li, M.; Zhang, Y.; Xu, H.-M.; Zhang, X.-M. Tri(pyridinyl)pyridine Viologen-Based Kagome Dual Coordination Polymer with Selective Chromic Response to Soft X-ray and Volatile Organic Amines. *Inorg. Chem.* **2020**, *59*, 9047−9054.

(8) Xie, J.; Hou, H.; Lu, H.; Lu, F.; Liu, W.; Wang, X.; Cheng, L.; Zhang, Y.; Wang, Y.; Wang, Y.; Diwu, J.; Hu, B.; Chai, Z.; Wang, S. Photochromic Uranyl-Based Coordination Polymer for Quantitative and On-Site Detection of UV Radiation Dose. *Inorg. Chem.* **2023**, *62*, 15834−15841.

(9) Zhao, J.; Qu, X.; Wang, J.; Yan, B. Photophysical Tuning of Viologen-Based Metal−Organic Framework Hybrids via Anion Exchange and Chemical Sensing on Persulfate ($S_2O_8^{2-}$). *Ind. Eng. Chem. Res.* **2019**, *58*, 18533−18539.

(10) Feng, S.; Shang, Y.; Wang, Z.; Kang, Z.; Wang, R.; Jiang, J.; Fan, L.; Fan, W.; Liu, Z.; Kong, G.; Feng, Y.; Hu, S.; Guo, H.; Sun, D. Fabrication of Hydrogen-Bonded Organic Framework Membrane through Solution Processing for Pressure-Regulated Gas Separation. *Angew. Chem., Int. Ed.* **2020**, *59*, 3840−3845.

(11) Chen, W.-G.; Chen, Z.-J.; Zhang, L.; Wang, B.; Lin, Z.-Z.; Cao, R.; Wang, W.-R.; Chen, Y.; Wang, Y. Reversible, photoresponsive, dynamic wide-range emission color from polymer-matrixed naphthalene diimide single-luminogen. *Chem. Eng. J.* **2022**, *432*, No. 134411.

(12) Shi, Y.-S.; Yang, D.-D.; Xiao, T.; Xia, Z.-G.; Fang, Y.-H.; Zheng, X.-J. Photoinduced multi-color emission of naphthalenediimide radical in different solvents and dynamic anti-counterfeiting film. *Chem. Eng. J.* **2023**, *472*, No. 145152.

(13) He, Z.; Li, Y.; Wu, H.; Yang, Y.; Chen, Y.; Zhu, J.; Li, Q.; Jiang, G. Novel Stimuli-Responsive Spiropyran-Based Switch@HOFs Materials Enable Dynamic Anticounterfeiting. *ACS Appl. Mater. Interfaces.* **2022**, *14*, 48133−48142.

(14) Liu, J.-J.; He, C.; Liu, T.; Liu, J.; Xia, S.-B. Two Photochromic Hybrid Materials Assembled from Naphthalene Diimide as Photocatalysts for the Degradation of Carcinogenic Dye Basic Red 9 Under Visible Light. *J. Mol. Struct.* **2021**, *1243*, No. 130804.

(15) Liu, W.; Lu, H.; Zhang, Y.; Huang, H.; Zheng, X.; Liu, Y.; Wu, Y.; Xu, X. Enhancing the Performance of Organic Solar Cells by Modification of Cathode with a Self-Assembled Monolayer of Aromatic Organophosphonic Acid. *Chin, Chem. Lett.* **2023**, *34*, No. 107495.

(16) Wei, Y.-Q.; Sun, C.; Chen, Q.-S.; Wang, M.-S.; Guo, G.-C. Significant Enhancement of Conductance of a Hybrid Layered Molybdate Semiconductor by Light or Heat. *Chem. Commun.* **2018**, *54*, 14077−14080.

(17) Shan, Z.; Xiao, J.-Z.; Wu, M.; Wang, J.; Su, J.; Yao, M.-S.; Lu, M.; Wang, R.; Zhang, G. Topologically Tunable Conjugated Metal−Organic Frameworks for Modulating Conductivity and Chemiresistive Properties for NH_3 Sensing. *Angew. Chem., Int. Ed.* **2024**, *63*, No. 202401679.

(18) Lv, Y.; Ke, S.-W.; Gu, Y.; Tian, B.; Tang, L.; Ran, P.; Zhao, Y.; Ma, J.; Zuo, J.-L.; Ding, M. Highly Efficient Electrochemical Nitrate Reduction to Ammonia in Strong Acid Conditions with Fe_2M-Trinuclear-Cluster Metal−Organic Frameworks. *Angew. Chem., Int. Ed.* **2023**, *62*, No. 202305246.

(19) Pal, S. C.; Das, M. C. Superprotonic Conductivity of MOFs and Other Crystalline Platforms Beyond 10^{-1} S cm^{-1}. *Adv. Funct. Mater.* **2021**, *31*, No. 2101584.

(20) Liu, G.; Yuan, Y. D.; Wang, J.; Cheng, Y.; Peh, S. B.; Wang, Y.; Qian, Y.; Dong, J.; Yuan, D.; Zhao, D. Process-Tracing Study on the Postassembly Modification of Highly Stable Zirconium Metal−Organic Cages. *J. Am. Chem. Soc.* **2018**, *140*, 6231−6234.

(21) Khan, N. A.; Luo, M.; Zha, X.; Azad, C. S.; Lu, J.; Chen, J.; Fan, C.; Rahman, A. U.; Olson, M. A.; Jiang, Z.; Wang, D. Water/Vapor Assisted Fabrication of Large-Area Superprotonic Conductive Covalent Organic Framework Membranes. *Small* **2023**, *19*, No. 2303131.

(22) Yang, Y.; He, X.; Zhang, P.; Andaloussi, Y. H.; Zhang, H.; Jiang, Z.; Chen, Y.; Ma, S.; Cheng, P.; Zhang, Z. Combined Intrinsic and Extrinsic Proton Conduction in Robust Covalent Organic Frameworks for Hydrogen Fuel Cell Applications. *Angew. Chem., Int. Ed.* **2020**, *59*, 3678.

(23) Tao, S.; Zhai, L.; Wonanke, A. D. D.; Addicoat, M. A.; Jiang, Q.; Jiang, D. Confining H_3PO_4 Network in Covalent Organic Frameworks Enables Proton Super Flow. *Nat. Commun.* **2020**, *11*, 1981.

(24) Cao, L.; Wu, H.; Cao, Y.; Fan, C.; Zhao, R.; He, X.; Yang, P.; Shi, B.; You, X.; Jiang, Z. Weakly Humidity-Dependent Proton-Conducting COF Membranes. *Adv. Mater.* **2020**, *32*, No. 2005565.

(25) Chen, X.; Geng, K.; Liu, R.; Tan, K. T.; Gong, Y.; Li, Z.; Tao, S.; Jiang, Q.; Jiang, D. Covalent Organic Frameworks: Chemical

Approaches to Designer Structures and Built-in Functions. *Angew. Chem., Int. Ed.* **2020**, *59*, 5050−5091.

(26) Wang, M.-M.; Cai, J.-J.; Lun, H.-J.; Lv, M.-G.; Zhang, J.-Q.; Andra, S.; Li, B.; Dang, D.-B.; Bai, Y.; Li, Y.-M. Design and Analysis of POM-Guanidine Compounds: Achieving Ultra-High Single-Crystal Proton Conduction. *Adv. Funct. Mater.* **2024**, *34*, No. 2311912.

(27) Cao, X.-J.; Cao, L.-H.; Bai, X.-T.; Hou, X.-Y.; Li, H.-Y. An Ultra-Robust and 3D Proton Transport Pathways iHOF with Single-Crystal Superprotonic Conductivity Around 0.4 S cm^{-1}. *Adv. Funct. Mater.* **2024**, *34*, No. 2409359.

(28) Bai, X.-T.; Cao, L.-H.; Zhao, F.; Li, S.-H. Arylsulfonate Ionic Hydrogen-Bonded Organic Frameworks Enable Highly Stable and Superprotonic Conductivity for Enhancing Direct Methanol Fuel Cells. *ACS Mater. Lett.* **2024**, *6*, 3351−3357.

(29) Zhao, F.; Cao, L.-H.; Bai, X.-T.; Chen, X.-Y.; Yin, Z. Application of Ionic Hydrogen-Bonded Organic Framework Materials in Hybrid Proton Exchange Membranes. *Cryst. Growth Des.* **2023**, *23*, 1798−1804.

(30) Bai, X.-T.; Cao, L.-H.; Chen, X.-Y.; Li, S.-H.; Zhang, J.-H. Dimethylamine-Tuned guanidinium Arylphosphonate iHOFs and Superprotonic Conduction Nafion Hybrid Membranes for DMFCs. *Chem. Eng. J.* **2024**, *487*, No. 150747.

(31) Lin, Z.-J.; Mahammed, S. A R; Liu, T.-F.; Cao, R. Multifunctional Porous Hydrogen-Bonded Organic Frameworks: Current Status and Future Perspectives. *ACS Cent. Sci.* **2022**, *8*, 1589−1608.

(32) Chen, S.; Ju, Y.; Zhang, H.; Zou, Y.; Lin, S.; Li, Y.; Wang, S.; Ma, E.; Deng, W.; Xiang, S.; Chen, B.; Zhang, Z. Photo Responsive Electron and Proton Conductivity within a Hydrogen-Bonded Organic Framework. *Angew. Chem., Int. Ed.* **2023**, *62*, No. e202308418.

(33) Wei, W.; He, L.; Han, G.; Lu, Y.; Shi, S.; Yuan, Z.; Wang, X.; Li, Y.; Chen, B.; Zhang, Z.; Xiang, S. Stimulus-Responsive Hydrogen-Bonded Organic Frameworks: Construction Strategies, Research Progress and Applications. *Coord, Chem. Rev.* **2024**, *507*, No. 215760.

(34) Lin, R.-B.; He, Y.; Li, P.; Wang, H.; Zhou, W.; Chen, B. Multifunctional Porous Hydrogen-Bonded Organic Framework Materials. *Chem. Soc. Rev.* **2019**, *48*, 1362−1389.

(35) Lin, R.-B.; Chen, B. Hydrogen-Bonded Organic Frameworks: Chemistry and Functions. *Chem.* **2022**, *8*, 2114−2135.

(36) Song, X.; Wang, Y.; Wang, C.; Wang, D.; Zhuang, G.; Kirlikovali, K. O.; Li, P.; Farha, O. K. Design Rules of Hydrogen-Bonded Organic Frameworks with High Chemical and Thermal Stabilities. *J. Am. Chem. Soc.* **2022**, *144*, 10663−10687.

(37) Wang, B.; Lin, R.-B.; Zhang, Z.; Xiang, S.; Chen, B. Hydrogen-Bonded Organic Frameworks as a Tunable Platform for Functional Materials. *J. Am. Chem. Soc.* **2020**, *142*, 14399−14416.

(38) Zhang, Z.; Ye, Y.; Xiang, S.; Chen, B. Exploring Multifunctional Hydrogen-Bonded Organic Framework Materials. *Acc. Chem. Res.* **2022**, *55*, 3752−3766.

(39) Song, Y.-J.; Xie, L.-X.; Sang, Y.-L.; Zhang, Y.-H.; Li, Z.-F.; Li, G. Ultrahigh Proton Conductivity of Four Ionic Hydrogen-Bonded Organic Frameworks Based on Functionalized Terephthalates. *J. Colloid Interface Sci.* **2024**, *674*, 1058−1070.

(40) Hisaki, I.; Chen, X.; Takahashi, K.; Nakamura, T. Designing Hydrogen-Bonded Organic Frameworks (HOFs) with Permanent Porosity. *Angew. Chem., Int. Ed.* **2019**, *58*, 11160−11170.

(41) Hori, Y.; Dekura, S.; Sunairi, Y.; Ida, T.; Mizuno, M.; Mori, H.; Shigeta, Y. Proton Conduction Mechanism for Anhydrous Imidazolium Hydrogen Succinate Based on Local Structures and Molecular Dynamics. *J. Phys. Chem. Lett.* **2021**, *12*, 5390−5394.

(42) Moi, R.; Ghorai, A.; Maity, K.; Banerjee, S.; Biradha, K. Correlation of Structures with Proton Conductivity of 1D Coordination Polymers: Higher Proton Conductivity Due to Synergy of Encapsulated Sulfate Ions and Water Molecules. *Cryst. Growth Des.* **2022**, *22*, 7215−7220.

(43) Zhou, B.; Cao, L.-H.; Li, B.-S.; Chen, X.-Y.; Bai, X.-T. Ionic Hydrogen-Bonded Organic Frameworks with a Two-Photon Synergistic Color Change and Their Information Encryption. *ACS Appl. Mater. Interfaces* **2024**, *16*, 58931−58939.

(44) Zhou, Y.-N.; Wang, L.; Yu, J.-H.; Ding, T.-Y.; Zhang, X.; Jiao, C.-Q.; Li, X.; Sun, Z.-G.; Zhu, Y.-Y. Two Stable Cd-MOFs as Dual-Functional Materials with Luminescent Sensing of Antibiotics and Proton Conduction. *Inorg. Chem.* **2022**, *61*, 20111−20122.

(45) Ding, L.; Song, X.; Wang, L.; Zhao, Z. Enhancing Proton Conductivity of Polybenzimidazole Membranes by Introducing Sulfonate for Vanadium Redox Flow Batteries Applications. *J. Membr. Sci.* **2019**, *578*, 126−135.

(46) Yu, Y.; Zeng, Z.; Gao, X.; Xiong, C.; Zhu, H.; Cen, H.; Zheng, X.; Liu, Q.; Hu, T.; Wu, C. A Maximization of the Proton Conductivity of Sulfonated Poly(Ether Ether Ketone) with Grafted Segments Containing Multiple, Flexible Propanesulfonic Acid Groups. *Macromol. Rapid Commun.* **2023**, *44*, No. 2200926.

(47) Zhao, F.; Cao, L.-H.; Ji, C. Proton Conduction of an Ionic HOF with Multiple Water Molecules and Application as a Membrane Filler in Direct Methanol Fuel Cells. *J. Mater. Chem. C* **2023**, *11*, 15288−15293.

(48) Lv, X.-W.; Weng, C.-C.; Zhu, Y.-P.; Yuan, Z.-Y. Nanoporous Metal Phosphonate Hybrid Materials as a Novel Platform for Emerging Applications: A Critical Review. *Small* **2021**, *17*, No. 2005304.

(49) Huynh, R. P S; Evans, D. R.; Lian, J. X.; Spasyuk, D.; Siahrostrami, S.; Shimizu, G. K H. Creating Order in Ultrastable Phosphonate Metal-Organic Frameworks via Isolable Hydrogen-Bonded Intermediates. *J. Am. Chem. Soc.* **2023**, *145*, 21263−21272.

(50) Xing, X.-S.; Sun, C.; Liu, L.; Wang, M.-S.; Guo, G.-C. Light-Responsive Proton Conductor: Record High Gain of Proton Conductivity Achieved by Photoinduced Electron-Transfer Strategy. *CCS Chem.* **2021**, *3*, 50−57.

(51) Bhosale, S. V.; Kobaisi, M. A.; Jadhav, R. W.; Morajkar, P. P.; Jones, L. A.; George, S. Naphthalene Diimides: Perspectives and Promise. *Chem. Soc. Rev.* **2021**, *50*, 9845−9998.

(52) Cheng, H.-P. The Motion of Protons in Water−Ammonia Clusters. *J. Chem. Phys.* **1996**, *105*, 6844−6855.

(53) Pomes, R.; Roux, B. Structure and Dynamics of a Proton Wire: Atheoretical Study of H^+ Translocation along the Single-File Water Chain in the Gramicidin A Channel. *Biophys. J.* **1996**, *71*, 19−39.